PROGNOSTICS OF AEROSPACE ELECTROMECHANICAL ACTUATORS USING THE FAILURE MAPS TECHNIQUE

PROGNOSTICS OF AEROSPACE ELECTROMECHANICAL ACTUATORS USING THE FAILURE MAPS TECHNIQUE

Alessandro Aimasso* Leonardo Baldo* Matteo Dalla Vedova* Paolo Maggiore*

* Department of Mechanical and Aerospace Engineering, Politecnico di Torino, Turin, Italy

ABSTRACT

The gradual deployment of Electro Mechanical Actuators (EMAs) as primary flight controls actuators, driven by the "more electric" approach, must be paired up with a solid prognostic background in order to overcome the limited experience and to support the system during his lifecycle. In fact, assessing EMAs actual states thanks to Prognostic and Health Monitoring (PHM) systems and detecting potential failures is crucial to guarantee the compliance to the relative safety requirements. The research activity described in this paper focuses on the development of a model-driven deterministic methodology based on Failure Modes Maps (FMMs). Thanks to data obtained through a Numerical Test Bench (NTB) and a Simplified Model (SM), the proposed prognostic algorithm is proved capable of detecting and identifying the source and magnitude of two different failures: rotor eccentricity and increased friction. After a short description of the implemented models and a general overview of typical EMA failure modes as well as FMMs development, the proposed algorithm is explained in detail. This is followed by a comprehensive study of the two simulated failures as well as the creation of the relative FMMs. Finally, the proposed prognostic algorithm is successfully applied on the obtained FMMs.

Keywords: Prognostics, Failure Map, EMA, Failure, PHM

1 INTRODUCTION

The increasing adoption of EMAs in the aerospace sector, together with the deployment of alternative propulsion technologies, has always been one of the pivotal aspects necessary to facilitate the implementation of the "*more electric aircraft*" (MEA) design philosophy. In fact, the installation of EMAs instead of traditional hydraulic actuators offers a plethora of benefits, among which the downsizing (or complete removal) of the hydraulic systems is one of the most rewarding. The removal of this extensive subsystem can lead to a significant weight reduction as well as a drastic cut to maintenance and operations costs. It is therefore evident why, in the last decades, a strong interest in the "*more electric*" trend has been driving the aerospace sector. However, at the same time, the gradual change towards MEA architectures is slowed down by their critical failure modes and limited experience with these systems.

In fact, only in recent times EMAs have been employed as secondary flight controls (FC) actuators and as primary flight controls actuator in small vehicles [1,2].

EMAs fault modes are often critical and some of them, such as the mechanical jamming of the actuator or some generic electrical failures could lead to hazardous or catastrophic failure condition, especially if EMAs are intended as primary FC actuators for which safety is the number one priority. Usually, FC are designed following a safe-life philosophy, thus not involving the system actual state at all and scheduling maintenance checks relying on "*a priori*" analyses which do not take into account any initial production flaw that could result in sudden failures in the long run [3]. In fact, equipment failures (especially in EMAs) are often unpredictable and the effect could not be visible until the consequences are already severe. A hidden failure could remain undetectable if no specific and targeted sensor equipment and appropriate algorithms are provided.

It is clear that long-established approaches to design and maintenance are unacceptable since the aforementioned failure modes must be prevented from happening at all and a pure and simple replacement of hydraulic actuators by EMAs is not sufficient. Likewise, redundancy is implausible due to the added weight and the lower basic reliability: here arises the need of an additional "*level*" of safety.

A system capable of detecting and identifying the failure is therefore critical to guarantee the acceptable safety standards. This is when Prognostics and Health Management (PHM) systems prove useful: analyzing the systems and component behaviours thanks to appropriate sensors, detecting even small-scale changes in the systems parameters, identifying what is happening and, in the more advanced methods, adapting and replanning the mission [4,5,6].
Thanks to complex algorithms and procedures, prognostics is able to carry out the so-called Fault Detection and Identification (FDI) step, essential to intercept the failure before the materialization of the relative failure condition and their respective harmful consequences. Prognostics is also able to predict the effect of a failure and assess its possible propagation at a sub-system and system level, estimating the Remaining Useful Life [7,8].
On this basis, Condition Based Maintenance (CBM) strategies could also be approached [9]. Additional benefits strictly related to the implementation of prognostic strategies could be: an increase of the system availability, a leaner approach to Integrated Logistic Support (ILS) as well as a general improvement of mission readiness and a reduction of Life Cycle Costs (LCC) [10,11].
In general, prognostic approaches are data driven [12] or, like the one proposed in this article, based on models [13,14]. In fact, the proposed methodology is based on a Simplified Model (SM), capable of medium to high accuracy with low computational time.
Actually, in this paper, two different models are presented along with the relative peculiarities: a Numerical Test Bench (NTB) and a Simplified Model (SM). The former is a high-fidelity model which has been used by the authors as a test bench emulator; in other words, it has been used as a reference model. The latter is a low fidelity model which is employed inside the prognostic loop.
The authors tested a peculiar prognostic methodology, based on failure mode maps (FMMs), capable of detecting and identifying two different failures: rotor eccentricity and increased friction in the transmission.
These are among the most frequent and harmful failure modes in EMAs systems. Failure modes maps, often used in materials and structural analyses [15,16,28], are presented in this work as a quick and easy to read method to identify possible faults among a restricted number of hypotheses.

2 EMA FAILURE MODES

EMAs are very complex systems where electrical, mechanical and electronic components work together to provide seamless motion at the output shaft.
The presence of such a variety of parts inevitably reduces the system inherit reliability, causing a very high number of possible failure modes [4] which can be assessed thanks to safety analyses.

Balaban et al. [17,18] carried out extensive FMECA studies to determine the most common EMA failure modes (e.g. mechanical/structural, motor faults and electric failures), assess the relative criticality and provide a statistical base for future analyses.
In this paper only two mechanical failure modes were selected and injected in our experiments: eccentricity and increased friction.
In fact, mechanical and structural faults are the main source of concern for EMAs and they are the most demanding ones to build a prognostic algorithm upon.
Furthermore, referring to the tables presented in [17], these faults present quite a high risk (medium-high criticality number) concerning safety and they represent some of the main technical challenges.
Moreover, there are several studies focused on the detection of rotor eccentricities and on friction estimations, given the extreme importance of these failures [20,21,22].

2.1 ECCENTRICITY

Rotor eccentricities represent one of the most harmful and investigated issue in electric motors. Among other effect, they play a major role in generating vibrations, creating electromagnetic noise injected in the system as well as mechanical and acoustic noise. [19]
The eccentricity in electrical machines is often referred as air-gap eccentricity: as the air gap is the radial distance between the stator core and the moving rotor, a potential eccentricity in the rotor inevitably reflects on the air gap magnitude around the mechanical angle.
In fact, eccentricity in electrical machines is commonly defined as a condition of unequal air gap between rotor and stator. The air gap is a key parameter for a correct motor operation and that is why a non-constant air gap around the mechanical angle is so deleterious for the overall performance of the electrical machine [23].
Air gap eccentricity is usually divided in static and dynamic eccentricity. In this work, the authors implemented the simulation of static eccentricity.

Static eccentricity is caused by a misalignment between the rotor axis and the stator axis. However, since the rotor is symmetric with respect to its own rotation axis, no mechanical vibration is produced and the positions of minimum and maximum air gap magnitude are fixed in time and space.
This defect can be caused by manufacturing defects or, more commonly, by the uneven wear of bearings and causes a general increase in the magnetic induction where the air gap is thinner, thus leading to a higher current consumption and irregularities during operations. On the other hand, dynamic eccentricity takes place when the center of the rotor does not coincide with the rotor center of rotation. Referring to Figure 1, Eq. 1 and 2 can be obtained:

$$g_0 = R_S - R_R \quad (1)$$

$$g'(\theta) = g_0(1 + \zeta \cdot cos(\theta)) \quad (2)$$

Where g_0 is the initial (nominal) air gap, R_S and R_R are the stator and rotor radii, ϑ is the rotation angle according to Figure 1 reference frame, g' is the actual air gap (involving eccentricity) and ζ is the eccentricity.

$$\zeta = \frac{(x_0)}{(R_S - R_R)} \quad (3)$$

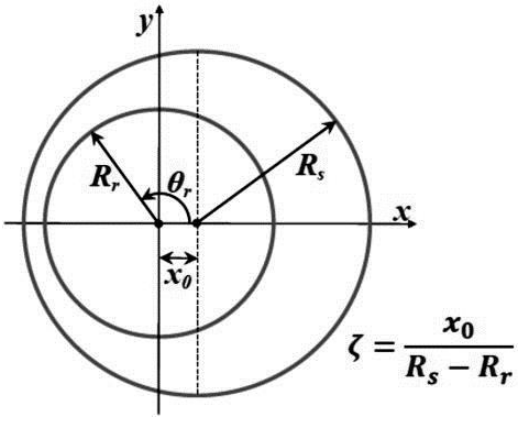

Figure 1 Static eccentricity reference system

Eq. 1,2,3 have been implemented in the models as shown in section 3.1.2.

2.2 FRICTION

In EMAs, loads are transferred between mechanical parts in contact with each other. In this case, friction acts only in limited gears regions and it is generated by micro-junctions formed due to surface roughness and due to the presence of very high local pressures and stresses [24].
This phenomenon causes serious threats to the system performance, safety and overall reliability. Usually, friction is taken into account and its effect are assessed during the design phase of mechanical systems, for instance considering newer technologies (e.g. harmonic drives, planetary gearboxes, ball screws).
Friction plays a relevant role in the stability and accuracy of controlled systems; hence its magnitude must be assessed in the controller tuning phase to achieve a resilient and robust control. On the other hand, various macroscopic detrimental effects due to friction may be: temperature increases, efficiency decreases and, above all, a wear of the parts in contact, leading to metallic particle in lubrication fluid too.
If friction conditions were to change during EMA operations, there could be a reduction in system accuracy or the introduction of unexpected and unwanted behaviour [26]. In fact, in the presence of proportional integrative control logic, unexpected friction magnitude could lead to limit cycles, due to the interplay for friction, inertia and the controller integrative branch or dynamic instabilities (e.g. stick-slip motion).
In the worst-case scenario, a jamming of the actuator may happen, causing hazardous or catastrophic failure conditions [22]. To sum up all that has been stated so far, detecting any failure related to a friction increase in EMA mechanical transmissions is key to create a satisfactory PHM system.

3 EMA MODELLING

The considered EMA is based on a linear, ball-screw actuator powered by a selected BLDC motor: the Faulhaber 4490H048BS. As stated before, a total of two modular EMA models has been developed and used in this work:

- The **NTB**, which is a highly detailed model, representing a simulated test bench. It is able to offer high fidelity reference data concerning nominal (NC) and non-nominal conditions in terms of positions, speed, currents, voltages etc. The throwback is a very long running time, hence a real-time implementation is unreasonable. This model proved useful for gathering an extensive database involving the desired nominal and non-nominal conditions.
- The **SM**, which is at the heart of the prognostic algorithm. The Simplified Model is a monitor model able to provide the authors with NC simulated data with an optimum trade-off between data details and computational costs. In fact, given its major role inside the prognostic methodology, running time is as important as data quality.

The two models have been calibrated using the motor datasheet, plausible inertial and mechanical data, thus obtaining an actuation dynamics that is intermediate between primary and secondary flight controls.
Both models are based on the pure Simulink implementation of physical formulas, strictly linking the model to the real-life situation.

3.1 NUMERICAL TEST BENCH (NTB)

The NTB main scheme is reported in Figure 2 and it can be divided into 3 main blocks:

- Controller block;
- Electro-mechanical model block;
- Motor dynamics block.

Moreover a "*Com*" block generates the different position commands (e.g. Step signal, Sinusoidal signal, Chirp signal) with custom parameters and the EMA Output block logs data into the *Matlab Workspace*.

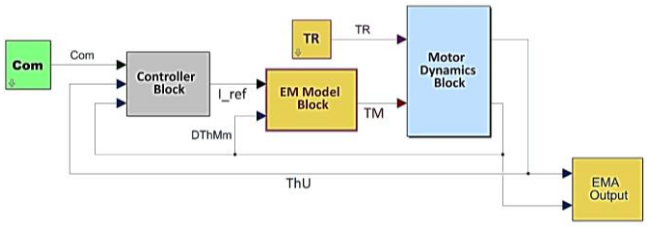

Figure 2 NTB Simulink model

3.1.1 Controller Block

The Controller Block takes as input the user angular position (*ThU*), motor angular velocity (*DThM*), and the signal command (*Com*).
Position error (*Err Pos*), defined as the difference between "*Com*" and "*ThM*", is passed to a pure proportional control loop composed of an amplifier and a saturation block, yielding a reference value for motor speed called "*W_ref*".
The angular velocity error (*Err_W*). is obtained by subtracting actual motor velocity (*DThM*) from this value.
The angular velocity error enters a PID inner speed control loop with integrative and proportional logic: by taking these two contributions into account, a motor torque reference value (*TM_ref*) is obtained.
The reference current, "*I_ref*", is obtained by "*TM_ref*" divided by the torque constant (*kt*) and is regulated by a saturation block to prevent thermal damage due to excessive circulation current.
It is worth noting that "*I_ref*" does not reflect the true value of circulating current in the three motor phases, but rather only serves as a reference value for appropriate phase commutation.

3.1.2 Electro-Mechanical (EM) Model Block

The BLDC motor is basically modelled as a three-phase star-connected system with three ohmic-inductive branches (Figure 4). This block shows two inputs:

- Reference current "*I ref*";
- Motor speed "*DthM*".

On the other hand, the output is the torque motor "*TM*", which is calculated in another sub-block starting from phase currents and CEMF coefficients.
This block is divided into six sub-blocks, whose details are explained below:

- **Reference current calculator block**. The actual motor position (*ThM*) is used to split the reference current "*I_ref"* into three different phase currents.

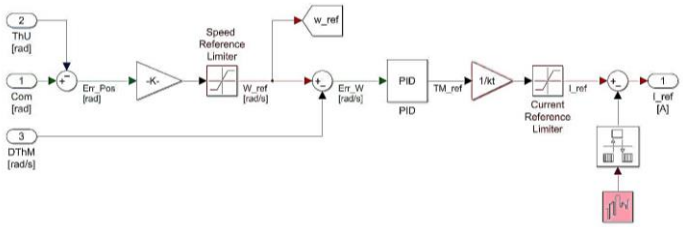

Figure 3 Controller Block

This is achieved thanks to three parallels "*Lookup blocks"*, one for each phase. *"Lookup blocks"* are elementary blocks which provide one dimensional linear interpolation depending on input data.

For each phase, a simplified rectangular time history is set: in this way, according to the motor position (*ThM*), each one of the three phases receives the right phased current value.
Each *"lookup block"* is set with a rectangular wave (with value of -1, +1 or 0) out of phase by 120° with each other.
The outputs of each *"Lookup block"* is then multiplied by "*I_ref"*, hence providing a 1x3 output vector with three rectangular currents correctly phased and with the same amplitude.
In other words, according to the motor angle, a time history of the phase currents is generated.

- **PWM block.** The reference current "*I_ref"* is compared with the three actual currents circulating in the three phases to obtain a simple feedback control. The three errors between the reference current and the actual currents are handled by three hysteresis blocks. These blocks are the easiest and less computationally intensive way to simulate fast PI controllers. The hysteresis control is actuated by switching the blocks output signal *on / off* and inserting a dead band. In other words, if the subtraction result is greater than $+HB$ (band-width) the output value is 1, while if the result is less than $-HB$ the output value is -1. Basically, if, in a given coil, current is requested, then the relative transistors are activated. If the difference falls into the bandwidth, transistors are switched-off and the block output value is 0. This is a fast and easy way to generate a high frequency PWM signal: to all intents and purposes, each hysteresis block outputs a high frequency square wave, hence modulating PWM duty cycle based on the error signal obtained by the difference between the actual current and the required current. These signals are then used to switch on or off the inverter.
- **Inverter block**. This subsystem has been implemented thanks to *SimScape* add-ons. De facto, the inverter block consists of a three phase H-bridge, modelled thanks to the multi-domain blocks offered by *SimScape*. The three Boolean signals, obtained through the hysteresis blocks, are assembled in a 1x6 signal vector along with their negated values. Then the signal is passed to the "*universal bridge*" which, as a result of internal algorithms, outputs three voltages: *A, B, C*.
- **Phase currents calculation block.** This block receives in input the voltages *A, B, C* and the counter electromotive forces coefficients *"ea", "eb", "ec"*. Phase currents and voltages are obtained thanks to three RL branches.

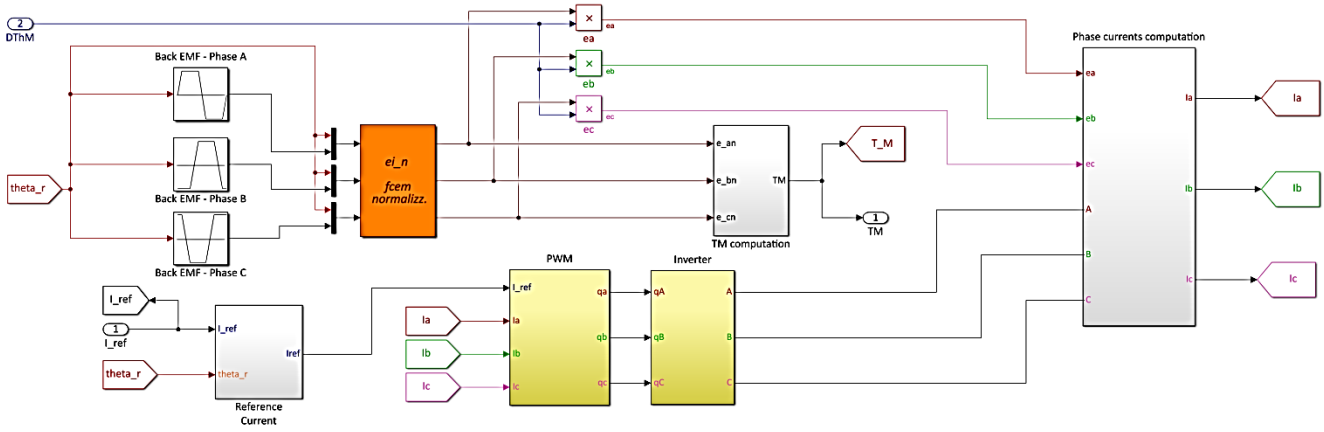

Figure 4 EM Model Block

Moreover, a single equivalent current based on Eq. 4 for BLDC is obtained:

$$I_{3eq} = \frac{1}{2}(|i_A| + |i_B| + |i_C|) \quad (4)$$

The equivalent current is then employed in the comparison between the NTB and the SM, where a single-phase approach is followed.
Voltage and current signals are filtered before they can be displayed.

- **CEMF computation block.** This block calculates instantaneous CEMF coefficients for each phase thanks to the motor position. The CEMF constant *"ke"* for each of the three phases is calculated, taking into account possible electrical failures too.
  Eq. 5 shows the law used to obtain the three normalized CEMF for the *i-th (1,2,3)* phase:

$$K_{fcem}(i) = K_e(i) \cdot u(2) \cdot [1 + (P > 1) \cdot \zeta \cdot \cos(\theta_r + \frac{2}{3}(i-1)\pi)] \quad (5)$$

  $Ke\ (i)$ is the nominal counter electromotive force coefficient without any fault injection; the coefficient is potentially different for each phase but practically equal if no short circuit failure is considered. P is the number of polepairs per each phase. The second part of the equation is used for taking into account the static eccentricity: ζ can vary from 0 to 0.5 (Eq. 3). θ_r is the rotor angle. It is clear that in nominal condition this value should be equal to zero, hence the CEMF coefficient is the nominal one. It is worth noting that, as stated before, this block outputs the normalized CEMF coefficient, the CEMF coefficients can be easily obtained by multiplying the normalized one with the rotor speed (Eq. 6).

$$e_i = e_i^n \cdot \dot{\theta_m} \quad (6)$$

- **Motor torque computation block.** Motor Torque is obtained following Eq. 7:

$$TM = \sum_{n=1}^{3} k_n \cdot I_n \quad (7)$$

  Which accounts for the three phases multiplied by the normalized CEMF coefficients. The torque is then estimated by summing together the three contributions. In fact, the three phase currents are multiplied by their respective "*ke*" and added up, since each phase gives a third of the total torque obtained, in nominal conditions.
  A saturation block is then added to limit the possible torque to reflect real core saturation behaviour.

3.1.3 Motor dynamics Block

This block receives in input the external torque and the motor torque previously obtained. On the other hand, motor position and speed are determined.
As a matter of fact, this sub model is able to simulate the motor-gears dynamics, whose mathematical formulation is shown in Eq. 8.

$$TM - TR = J_m \frac{d^2\theta_m}{dt^2} + C_m \frac{d\theta_m}{dt} \quad (8)$$

Where *TM* and *TR* are the motor and external torque values, J_m is the rotor inertia, θ_m is the motor position and C_m is the viscous coefficient. A sub-block is required to correctly model the second order mechanical system thanks to two distinct integrators.
This highly detailed dynamical simulation considers a wide range of non-linear phenomena affecting the actuator:

- Friction effects due to viscous forces are addressed thanks to a viscous coefficient C_m (dependent on speed);
- Inertial effects are addressed thanks to moments of inertia;

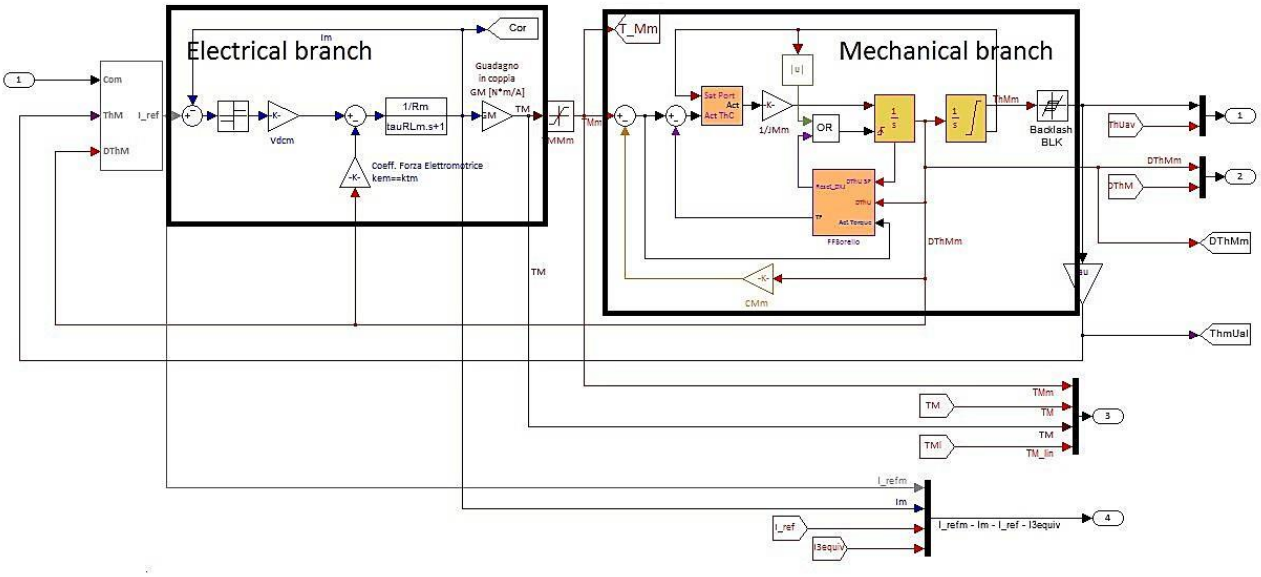

Figure 5 Simplified Model layout

- Dry friction effects are injected thanks to the Borello friction model [24], through the coefficient *FSJ*;
- Physical end-stops are addressed thanks to a saturation sub-block;
- Backlash effects are focused on thanks to a hysteresis band acting on the user shaft position.

3.2 SIMPLIFIED MODEL (SM)

The NTB is able to provide detailed behavioural simulation of an EMA, assessing his response accounting for physical interaction between elements and components. Despite the highly detailed response obtainable from the NTB, a lighter and quicker model is needed. In fact, prognostic algorithms require a real-time implementation, hence a model which is able to simulate nominal conditions in small amount of time is required.

On the other hand, to be coherent to the NTB, the SM must have the same overall structure and main functions. De facto, the SM is a stripped-out version of the NTB which can output its result in a time lap which is almost two orders of magnitude less than the NTB.

The main difference is the employment of an equivalent single-phase approach with an overall behaviour equivalent to the three-phase model but resulting in a significant reduction of the computation time [25].

The overall layout of the SM is shown in Figure 5 and a brief description of the ratio behind the model is reported. The interested reader can see [25] for a detailed analysis of the SM. The SM is employed only for nominal condition simulation, in order to compare failure affected parameters with nominal ones. Three main blocks are visible: the controller, the electrical branch and the mechanical branch.

3.2.1 Controller

As in the NTB, the SM controller receives in input the reference signal, the user position and the motor speed, whereas it outputs the reference current. However, the overall structure is lighter and simplified. The motor position is subtracted from the *"com"* signal, obtaining a reference speed via the proportional gain (limited by a saturation block in order to take into account mechanical restrictions). The reference speed is compared to the actual motor speed before being multiplied by another proportional gain that mimics the proportional gain of the PID controller in the reference model. The torque constant is then used to estimate the reference current. It should be noticed that a saturation block is also necessary in this branch to limit excessive currents.

3.2.2 Electrical branch.

The current is multiplied by a constant to convert the signal from a reference current into a reference voltage. A simplified *on-off* control applies ground or supply voltage to the motor depending on the comparison between the converted voltage setpoint "*I_ref"* and the actual voltage in the motor, obtained from the motor speed multiplied by the CEMF coefficient. This simplified *on-off* control is obtained thanks to the sign function and it follows the ratio shown in Eq. 9:

$$V_m = \begin{cases} +V_s, & I_m < I_{ref}, \\ 0, & I_m = I_{ref}, \\ -V_s, & I_m > I_{ref} \end{cases} \qquad (9)$$

Where V_m is the voltage given to the motor, V_s is the supply voltage, I_m is the motor current and I_{ref} is the reference current.

The current is determined using a specific transfer function, representing the RL circuit. This transfer function is based on:

$$V_m - k \cdot \omega = R \cdot I_m + L \cdot \frac{dI_m}{dt} \qquad (10)$$

Where k is the CEMF constant, ω is the motor speed, R represents the winding resistance and L represents the winding inductance. The current is finally multiplied by the torque constant to obtain the motor torque, which is then saturated.

3.2.3 Mechanical branch

The SM mechanical branch is the same as the NTB mechanical branch: torque calculated in the electrical branch is applied to the dynamic model, which accounts for motor inertia, viscous and friction effects, backlash, and non-linear end-stops. To solve the second-order dynamical system, the dynamical model utilizes two integrators.

3.3 MODELS COMPARISON

The NTB and the SM simulation trends in nominal conditions have been compared to check the goodness of SM results with respect to the NTB ones. The SM matches the NTB response for all observed parameters (torque, position and current), and for different inputs (step, ramp and sinusoidal waveform), demonstrating satisfactory behaviour. This is very important since the prognosis based on parameters estimation needs a good accuracy of the two models. As an example, Figure 6 shows the comparison between the models with a sinusoidal input (Semi-amplitude: 0.001 rad and 5 Hz).

4 FAILURE MODELLING AND FMMs

As stated before, a total of two failures have been considered: eccentricity and increased friction.
They have been implemented in the NTB:

- Eccentricity is simulated thanks to Eq. 5, where ζ can vary from 0 to 0.5;
- Increased friction is simply modelled by the increase of the friction coefficient FSJ, which is employed in the Borello friction model [24]. The friction varies from its nominal value to five time its nominal value.

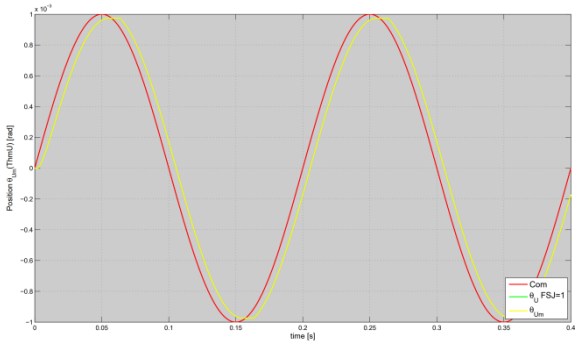

Figure 6 SM and NTB position trends.

4.1 FAILURE MODE MAPS

A failure map is a graphical representation of how a system-representative parameter varies as a function of two different types of faults. In other words, a failure map is a visual technique that employs a graph showing the trend of an observable system parameter plotted on the y-axis (e.g.
position error, overcurrent, speed error) as function of two
distinct failures (e.g. eccentricity, friction, short circuit, backlash).
Various failure maps concerning different parameters and failures can be obtained from extensive data-sets. Let us take into account one parameter *P* and two failures *G1* and G2. Taking into consideration the parameter *P* and one of the two failures *G1*, a single line can be obtained through multiple simulations showing the trend of the parameter *P* at different failure magnitudes *G1*. During this operation, the second failure *G2* has a constant magnitude. Now it is possible to repeat the same process with a different value of *G2*.
The result is similar to the one showed in Figure 5: a bundle of lines representing the same parameter *P* in different conditions determined by *G1* and *G2* magnitudes. The obtained graph is a failure map. A failure map, in more detail, shows

the first fault *G1* on the x-axis and the representative parameter *P* on the y-axis. Each map represents a set of curves P = f (G1) that have the second fault *G2* specified.
A good choice of *P* is critical to generate an effective failure map. This parameter should be a function of both *G1* and *G2* and should be extremely sensitive to changes in failure magnitude. Considering parameters showing a monotone trend as well as presenting lines that do not intersect each other as the given failures unfold is advisable to facilitate the prognostic process. In our case, various simulations have been performed to determine at least three sets of a parameter and two failures *(P1,G1,G2), (P2,G1,G2), (P3,G1,G2)* which could guarantee the aforementioned conditions along a wide range of failure magnitude variations. In fact, all these precautions allow for a more precise identification during the fault detection.
The selection of the appropriate input type (e.g. step, ramp, chirp) and parameter to monitor (e.g. speed or position error, currents) is another critical point.

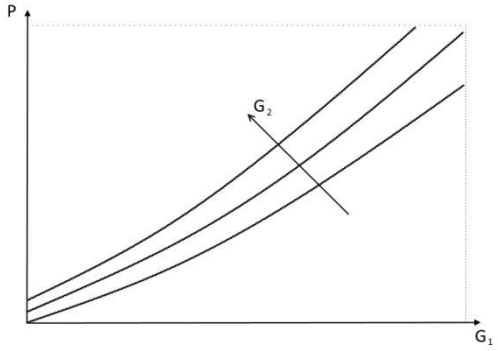

Figure 7 Failure map example

This means that, if the objective is to detect a failure by evaluating the dynamic response of a specific system, the positive outcome of the prognostic strategy (i.e. a correct failure identification) is dependable not only on the observable parameters but also on the input type. In other words, in order to have the best parameter estimation, a test campaign must be run and the optimum input for each parameter must be selected.
Considering the same parameter but approached with different input type leads to different failure map trends.

4.2 FAILURE MAPS CREATION

To obtain reliable failure maps, different and easily measurable parameters (*P*) shall be considered.
In particular, to create three failure maps independent of one another, the following quantities have been identified:

- Speed RMS Error;
- Current RMS Error;
- Starting Error.

For each of them, a specific failure map has been developed, considering as the first failure (*G1*) the friction and as the second failure (*G2*) the eccentricity.

4.2.1 First failure map

The first failure map is created by considering the Root Mean Square Error of the user speeds compared to the speed mean value. The parameter has been calculated from the analysis of a response to a step input.
In particular, a step input of 1 [rad] has been injected, with a simulation time of 0.8 s (a time which is enough to reach the regime speed). Hence, the model, involving progressive combined failures concerning eccentricity and friction, has been simulated. Based on these results, the effect of non- nominal eccentricity has been correlated to the amplitude variation of the oscillations around the mean value, while the friction directly changed the average speed.
The entity of friction and eccentricity could lead to different outcomes: indeed, for low friction values, the motor resulted still able to overcome resistance; whereas, when the eccentricity was too high, also friction effects became more important, as the motor is brought far from its nominal conditions. This behavior led strong support to consider the Root Mean Square Error of the user speed (compared to the steady state one) to obtain the first failure map. The parameter is therefore calculated as:

$$RMSE_{speed} = \sum_{t=1}^{n} \sqrt{\frac{\left(\bar{\dot{\theta}} - \dot{\theta}_t\right)^2}{n}} \qquad (11)$$

Where

- $\dot{\theta}_t$ is the user speed, evaluated at a certain time *t*,
- $\overline{\dot{\theta}}$ is the mean value of user speed at regime condition,
- *n* is the number of considered samples.

For increasing failure magnitudes, $RMSE_{speed}$ has been calculated and graphed. A monotonic trend is observed for different ζ values, with increasing FSJ: in this way the first failure map has been obtained.

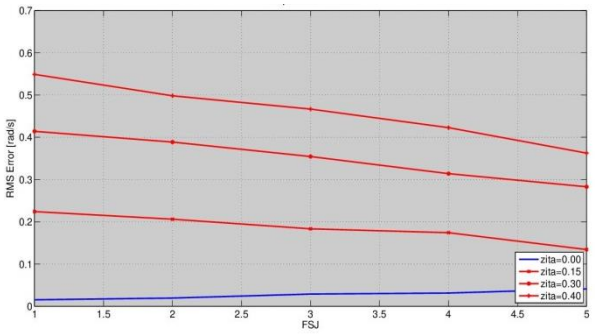

Figure 8 First failure map.

4.2.2 The second failure Map

A second simulation campaign has been performed by applying a sinusoidal command. A simulation time of 1 s was set, because it is deemed enough to observe an adequate number of complete sinusoidal waves in system responses.
The results showed a significative gap between current values in nominal and faulty condition with increasing friction, which resulted more influent if compared to the irregularity generated by the eccentricity.
So, the Root Mean Square error between phase currents has been calculated as:

$$RMSE_{current} = \sum_{t=1}^{n} \sqrt{\frac{\left(I_{3equiv} - I_m\right)^2}{n}} \qquad (22)$$

Where:

- I_{3equiv} is the equivalent single-phase current calculated for the three phases motor
- I_m is the phase current in monitor model
- *n* is the number of considered samples

For increasing failure condition $RMSE_{current}$ has been calculated and graphed observing a monotonic trend for different ζ values, with increasing FSJ: a second failure map has thus been obtained.

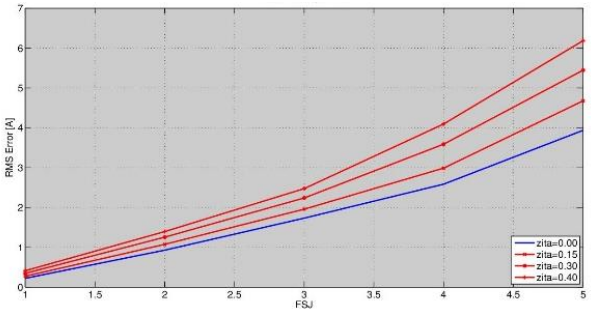

Figure 9 Second failure map.

4.2.3 The third failure map

Finally, a third set of simulations has been carried out with a ramp input with a simulation time of 1 s.
Considering different ζ values, the variation of position response has been analyzed, thus considering it as the parameter employed for the third failure map.
Looking at position response to ramp for several parameterized in FSJ, error at start has been evaluated, considering the command value when the system leaves the zero speed condition.

$$ERR_{norm} = \frac{Com_{speed \neq 0}}{ERR_{NC}} = \frac{ERR}{ERR_{NC}} \qquad (13)$$

Where $Com_{speed \neq 0}$ is the command value when system leaves zero speed condition. *Err* shows a monotone crescent trend with FSJ. Error normalized (13) respect to his nominal condition value has been graphed with FSJ in x-axis and parametrization in ζ, obtaining the third failure map. The map shows a quasi-linear monotone trends of error in function of FSJ, with slopes that increase with ζ

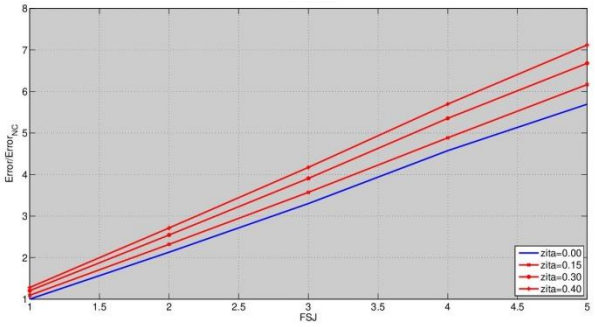

Figure 10 Third failure map.

5 PROPOSED METHODOLOGY

5.1 THE PROGNOSTIC ALGHORITM

The proposed prognostic technique described in this work is based on the use of the failure maps previously described. At first, it is crucial to underline that, to obtain results useful for prognostics, several failure maps are requested. This is the reason why, in this chapter, three failure maps, each one correlated to a different parameter, have been described. The proposed technique requires at least two different maps. The algorithm is structured as follows:

- The first failure map shall be considered. It has got, on the y-axis, the reference parameter *P1*. As already described, its current value *P1** is known: on the failure map, P1* is entered in the graph as y-axis.
- Using P1* value, a correspondent abscissa *G1** can be found, as shown by the figure 9. This represents the value of the first fault parameter. Moreover, each curve represented in the failure maps described different values of the second fault parameter *G2*: considering that usually more than one curve is intersected by the *P1** value, more *G1* intervals on the x-axis could be found (as shown in fig. 9, *G1** and *G1***).
- The second failure map is then considered. This takes into account the second parameter *P2*, and also in this case its value is known (*P2**). The procedure described at point 2 is now repeated, and another set of possible *G1* values is detected (figure 11)
- Once the possible intervals of values for *G1** have been defined for the first and the second failure maps, their intersection shall be considered, to define the final G1 interval. From this, it is now possible to define the interval of *G2* possible values.
- A combination of two failures affecting the system is so identified.

If this algorithm is performed by using more than two maps, it is possible to superimpose more intervals of failures, guaranteeing more accurate results.

When several maps are employed, each FMM has to be independent of one another: unrelated maps can be obtained considering three distinct parameters or different command inputs. By using three independent maps, i.e. reflecting three different characteristics, an accurate area containing the possible faults can be identified. When a third maps is considered, the procedure is the same employed for the second one, and also for the eventual successive.

5.2 CONCEPT OF OPERATIONS

A possible FDI method applicable to real life scenarios has been conceived. The pre-flight check phase is deemed to be the most appropriate one to perform a prognostic check (i.e. acquire, process and post-process data). Our concept of operations is fairly simple and it does not impact the aircraft availability nor its down-time at all. Before the flight, data useful to calculate enter parameters for the failure maps are gathered thanks to a specific sequence of inputs signals. This sequence has been carefully chosen to obtain clear results in accordance to Section 6. Failure maps specific for the employed EMA type are already created and loaded into a PHM computer on board or on specific ground hardware, hence the processing and post processing phase are not demanding at all. Once the data is gathered, the input parameters are loaded and matched with the appropriate failure maps. Through the matching of the three parameters P1, P2 and P3 on the respective failure

map, a possible fault area is detected as shown in Section 6. By performing a pre-flight test like the proposed one, an airline CAMO can optimize its maintenance strategy and assess the system real state before the flight just with some simple actuator movement sequence.

6 RESULTS AND DISCUSSION

The proposed methodology has been employed on the results given by the numerical test bench. The overall simulation performed by the model covered a time of 3 seconds, with the following commands sequence:

- a 0.50 s ramp input (slope 0.001 rad/s), with control surface slowly moving toward maximum deflection;
- a 0.35 s time lapse while the actuator returns to zero position;
- a 1.00 s sinusoidal input (semi-amplitude: 0.001 rad; frequency: 5 Hz), with control surface deflecting up and down around zero position;
- a 0.35 s time lapse while the actuator just brings back again to zero position by previous command stay static before next command;
- a 0.80 s step (of high amplitude: 1 rad), with the control surface which quickly goes to maximum deflection.

During the simulation, in the numerical test bench, a defined level of friction and static eccentricity were fixed and applied for the three different command inputs.
As already described, the data acquired are:

- speed θ_M
- current in phases I_{3equiv}
- position θ_U,

Once they are calculated, it is possible to obtain respectively the values of *P1**, *P2** and *P3**.
It is now feasible to apply the method developed for failure maps. Initially, various failure scenarios were simulated by defining eccentricity and friction values.
For each couple of fault friction and eccentricity, the parameters *P1**, *P2** and *P3** have been entered in the failure maps and the overall prognostic procedure was applied.
An example of the results is shown in the following figures. The figures 11 and 12 describe how the faulty values detected resulted to be an accurate estimation of the real fault levels acting on the actuator.

In failure maps the real and the estimated values are reported as follow:

- Red triangle represents the actual failure magnitude,
- Blue dot represents the detected failure magnitude.

More precisely, an error analysis for proposed examples (Table 1) has been conducted by calculating:

$$ERR_{\%} = 100\,\frac{Exact\ value - Detected\ value}{Exact\ value} \qquad (34)$$

The detected values of the two failures are calculated as the centroid of the area referred to x-axis (FSJ estimation) and y-axis (ζ estimation). As already happened for different evaluated failures, the algorithm gave good results, demonstrating the strength of the proposed deterministic prognostic method based on failure maps. It properly worked in several faulty condition simulated, proving the ability of algorithm to identify fault operational area (with a certain tolerance). The results obtained showed how this developed prognostic algorithm resulted to be sensible to

- failure maps definition,
- amplitude of bands parameter.

Table I - Comparison between real and detected data

Exact value		Detected value		Err%	
ζ	FSJ	ζ	FSJ	ζ	FSJ
0,3000	2,0000	0,3000	2,0607	0,0000	3,0350
0,1700	1,2000	0,1500	1,2652	11,7647	5,4333
0,1500	3,5000	0,1500	3,4936	0,0000	0,1829
0,2700	2,2000	0,2700	2,2275	0,0000	1,2500

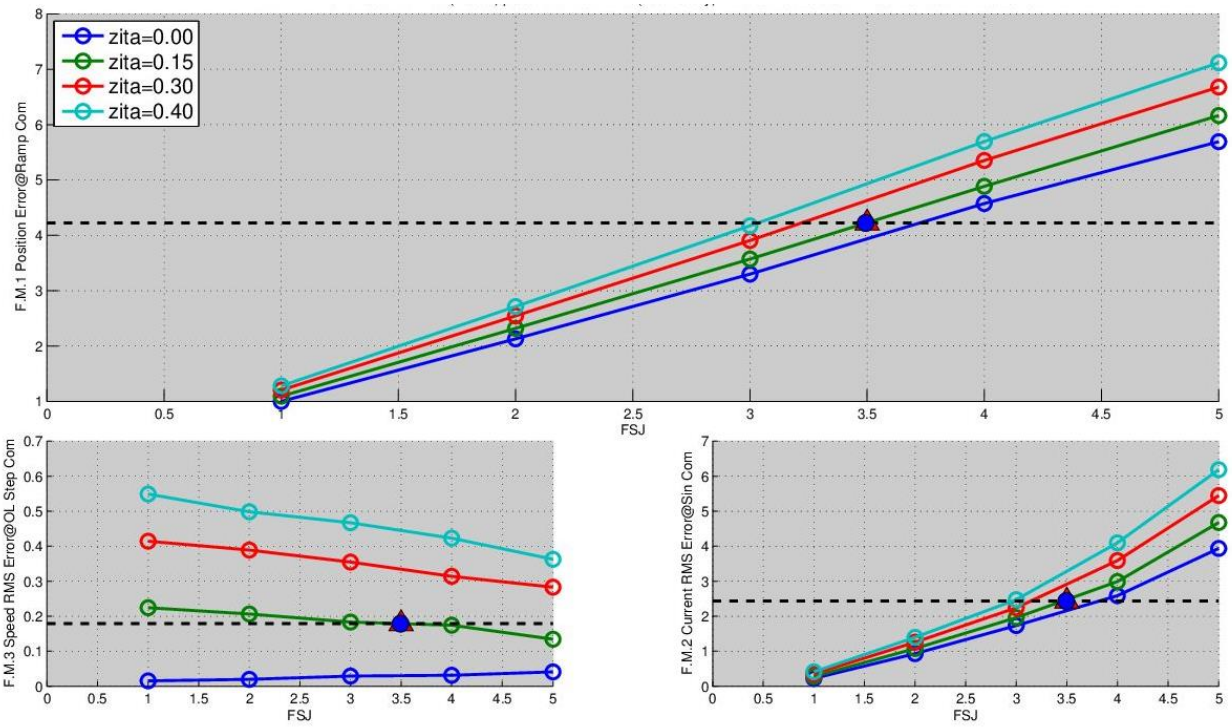

Figure 11 Example of prognostic algorithm implementation: FMMs

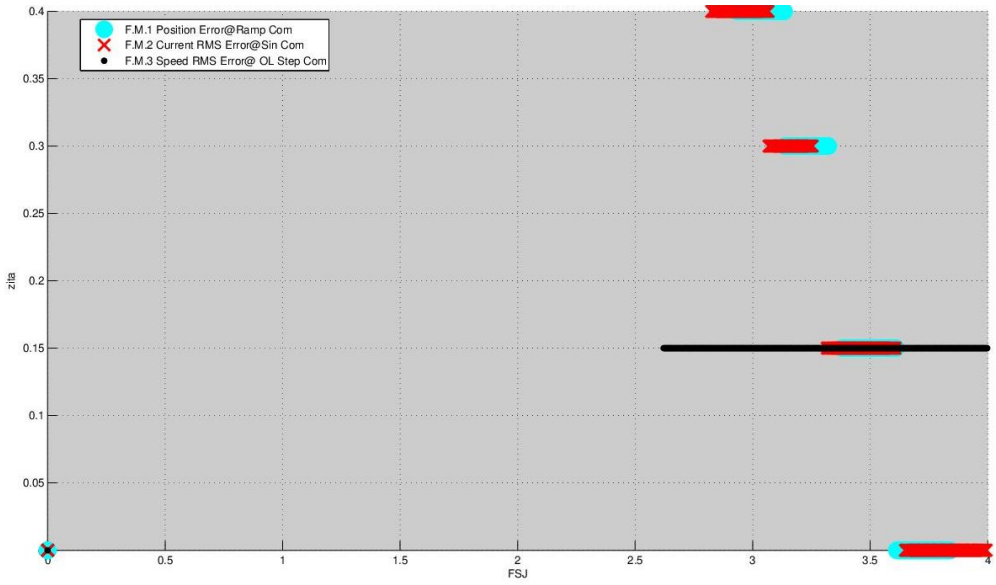

Figure 12 Example of prognostic algorithm implementation: failure identification.

Moreover, failure maps depend on number of simulations used to build it: a high number of simulations offers more detailed maps, improving the algorithm performances.

7 CONCLUSIONS

The results of this work are extremely positive and encouraging: a novel approach for prognostics for detection of gradually increasing faults on aircraft actuators was successfully established. Initially, a numerical test bench capable of simulating

progressive failures was created. Furthermore, this numerical model was greatly simplified by constructing a related monitoring model able to precisely describe the system reaction, giving the possibility of performing the needed tests.
The proposed prognostic algorithm estimates the extent of failures (i.e. the friction of the transmission and the static eccentricity of the rotor) by analyzing the dynamic response of the actuator to identify three parameters capable of detecting and identifying these failures. The dependence of these parameters on the health conditions of the EMA is depicted in failure maps.
It should be noted that, by monitoring the values of three common EMA parameters (e.g. phase current, angular position and rotor speed of the EMA motor), the authors' algorithm identifies with a suitable accuracy the health status of the system. Finally, these encouraging results may suggest that the proposed technique could be extended to investigate other occurrences, such as electrical failures, where the evolutions are typically very fast or instantaneous, making failure precursors difficult to identify and evaluate, especially when combined failures occur.

REFERENCES

[1] Derrien, J. C. and Sagem Défense Sécurité. Electromechanical actuator (EMA) advanced technologies for flight controls. *International congress of the aeronautical sciences*, Brisbane, pp. 1-10, 2012.

[2] Jensen S. C., Jenney G. D. and Dawson D., Flight test experience with an electromechanical actuator on the F-18 Systems Research Aircraft. *Proc. of 19th DASC Digital Avionics Systems Conference*. Proceedings (Cat. No.00CH37126), Vol. 1 pp. 2E3/1-2E310, 2000.

[3] Venkataraman R., Seiler P., Lukatsi, M., Vanek B., Reliability assessment of actuator architectures for unmanned aircraft, *Journal of Aircraft*, 2016.

[4] D. T. Paul Brian Hvass, Condition Based Maintenance For Intelligent Electromechanical Actuators, 2004.

[5] Chen, C., Brown, D., Sconyers, C., Vachtsevanos, G., Zhang, B., and Orchard, M. E. A. NET framework for an integrated fault diagnosis and failure prognosis architecture. *2010 IEEE AUTOTESTCON* (pp. 1-6). IEEE, 201.

[6] Byington, C. S., Watson, M., Edwards, D., and Stoelting, P. A model-based approach to prognostics and health management for flight control actuators. *IEEE aerospace conference proceedings* (IEEE Cat. No. 04TH8720) (Vol. 6, pp. 3551-3562). IEEE, 2014.

[7] Vachtsevanos G., Lewis F., Roemer M., Hess, R. Wu, B., *Intelligent Fault Diagnosis and Prognosis for Engineering Systems*, Wiley, 2006.

[8] Jihin R., Soffker, D., Beganovic N., Integrated prognostic model for RUL estimation using threshold optimization. *Structural Health Monitoring*, 2017.

[9] Benedettini, O., Baines, T. S., Lightfoot, H. W., AND Greenough, R. M. State-of-the-art in integrated vehicle health management. Proceedings of the Institution of Mechanical Engineers, Part G: *Journal of Aerospace Engineering*, 223(2), 157-170, 2009.

[10] Garcia Garriga, A., Ponnusamy S. S. and Mainini L., A multi-fidelity framework to support the design of More-Electric Actuation, *2018 Multidisciplinary Analysis and Optimization Conference, AIAA Aviation Forum*, (AIAA Paper 2018-3741), 2018

[11] Rosero, J. A., Ortega, J. A., Aldabas, E., and Romeral, L. A. R. L. (2007). Moving towards a more electric aircraft. *IEEE Aerospace and Electronic Systems Magazine*, 22(3), 3-9, 2007.

[12] Sutharssan, T., Stoyanov, S., Bailey, C., and Yin, C. Prognostic and health management for engineering systems: a review of the data-driven approach and algorithms. *The Journal of engineering*, 2015.

[13] Berri, P. C., Dalla Vedova, M. D., and Mainini, L. Learning for predictions: Real-time reliability assessment of aerospace systems. *AIAA Journal*, 60(2), 566-577, 2022.

[14] Battipede, M., Dalla Vedova, M. D. L., Maggiore, P., and Romeo, S. Model based analysis of precursors of electromechanical servomechanisms failures using an artificial neural network. *AIAA Modeling and Simulation Technologies Conference*, 2015.

[15] Petras, A., & Sutcliffe, M. P. F. Failure mode maps for honeycomb sandwich panels. *Composite structures, 44(4)*, 237-252, 1999.

[16] Sun, F., Lai, C., and Fan, H. Failure mode maps for composite anisogrid lattice sandwich cylinders under fundamental loads. *Composites Science and Technology*, 152, 149-158, 2017.

[17] Balaban, E., Bansal, P., Stoelting, P., Saxena, A., Goebel, K. F., and Curran, S. A diagnostic approach for electro-mechanical actuators in aerospace systems. *2009 IEEE Aerospace conference* (pp. 1-13), 2009.

[18] Balaban, E., Saxena, A., Goebel, K., Byington, C. S., Watson, M., Bharadwaj, S., and Smith, M. Experimental data collection and modeling for nominal and fault conditions on electro-mechanical actuators. *Annual Conference of the PHM Society* (Vol. 1, No. 1), 2009.

[19] Rezig, A., Mekideche, M. R., & Djerdir, A. Effect of rotor eccentricity faults on noise generation in permanent magnet synchronous motors. *Progress in Electromagnetics Research C*, 15, 117-132, 2010.
[20] Rajagopalan, S. Detection of rotor and load faults in brushless DC motors operating under stationary and non-stationary conditions. Georgia Institute of Technology, 2006.
[21] Zhu, Z. Q. and Howe D. Electromagnetic noise radiated by brushless permanent magnet DC drives 6th *IEMDC International Conference on Electrical Machines and Drives*, (Conf. Publ. No. 376) (pp. 606-611).Oxford, UK, September 1993
[22] Quattrocchi G., Iacono A., Berri PC., Dalla Vedova M. D. and Maggiore P. A new method for friction estimation in EMA transmissions. *Actuators*; Vol. 10 No. 8:194, 2021.
[23] Dorrell, D. G., Thomson, W. T., and Roach, S. Analysis of airgap flux, current, and vibration signals as a function of the combination of static and dynamic airgap eccentricity in 3-phase induction motors. *IEEE Transactions on Industry applications*, 33(1), 1997.
[24] Borello, L. and Dalla Vedova, M. D. A dry friction model and robust computational algorithm for reversible or irreversible motion transmissions. *International Journal of Mechanics and Control*, Vol. 13, No. 2, pp. 37–48, 2012.
[25] Berri, P. C. (2021). Design and development of algorithms and technologies applied to prognostics of aerospace systems. *PhD dissertatio*n https://iris.polito.it/handle/11583/2927464
[26] Dalla Vedova, M. D. L., Maggiore, P., Pace, L. and Desando, A. Evaluation of the correlation coefficient as a prognostic indicator for electromechanical servomechanism failures. *International Journal of Prognostics and Health Management*, 6(1), 2015.
[27] Romano A, Modelli per la prognostica delle avarie multiple di comandi di volo primari, *Tesi di Laurea Magistrale*, Politecnico di Torino, 2011
[28] Greco, A., Sorce, A., Littwin, R., Costamagna, P., and Magistri, L. (2014). Reformer faults in SOFC systems: Experimental and modeling analysis, and simulated fault maps. *International Journal of Hydrogen Energy*, 39(36), 21700-21713, 2014.